Thermo-hydro-mechanical modeling of geothermal energy systems in deep mines
Uncertainty quantification and design optimization

Zhang, Le; Dieudonné, Anne Catherine; Daniilidis, Alexandros; Dong, Longjun; Cao, Wenzhuo; Thibaut, Robin; Tas, Luka; Hermans, Thomas

DOI
10.1016/j.apenergy.2024.124531

Publication date
2024

Document Version
Final published version

Published in
Applied Energy

Citation (APA)
Zhang, L., Dieudonné, A. C., Daniilidis, A., Dong, L., Cao, W., Thibaut, R., Tas, L., & Hermans, T. (2024). Thermo-hydro-mechanical modeling of geothermal energy systems in deep mines: Uncertainty quantification and design optimization. *Applied Energy*, *377*, Article 124531. https://doi.org/10.1016/j.apenergy.2024.124531

Applied Energy 377 (2025) 124531

Contents lists available at ScienceDirect

Applied Energy

journal homepage: www.elsevier.com/locate/apenergy

Thermo-hydro-mechanical modeling of geothermal energy systems in deep mines: Uncertainty quantification and design optimization

Le Zhang [a,b,*], Anne-Catherine Dieudonné [b], Alexandros Daniilidis [b], Longjun Dong [c], Wenzhuo Cao [d], Robin Thibaut [a,e], Luka Tas [a], Thomas Hermans [a]

[a] Department of Geology, Ghent University, Ghent, Belgium
[b] Faculty of Civil Engineering and Geosciences, Delft University of Technology, Delft, The Netherlands
[c] School of Resources and Safety Engineering, Central South University, Changsha, China
[d] Department of Earth Sciences, Utrecht University, Utrecht, The Netherlands
[e] Lawrence Berkeley National Laboratory, Berkeley, CA, USA

GRAPHICAL ABSTRACT

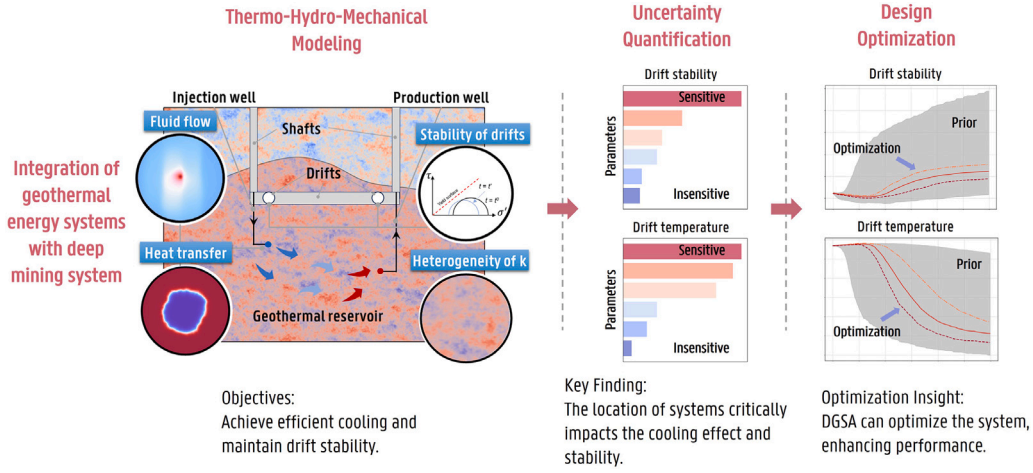

ARTICLE INFO

Keywords:
Deep geothermal energy
Thermo-hydro-mechanical modeling
Sensitivity analysis
Uncertainty quantification

ABSTRACT

Geothermal energy extraction through deep mine systems offers the potential to reduce the cost of geothermal systems while meeting the cooling needs of deep mines. However, the injection of cold water into the subsurface triggers strongly coupled thermo-hydro-mechanical (THM) processes that can affect the stability of underground excavations. This study evaluates the impact of geothermal energy extraction on the temperature and stability of a deep mine. By quantifying the sensitivity of the mine temperature and stability to various parameters, we propose a scheme to optimize geothermal energy production, while achieving rapid mine cooling and maintaining stability. We first evaluate the impact of geothermal operations on mine temperature and stability through THM numerical modeling. The simulations show that poro-elastic stress quickly affects mine stability, while thermal stress has a more significant impact on the long-term stability. We then use Distance-based Generalized Sensitivity Analysis (DGSA) to quantify parameter sensitivity. The analysis identifies the distance between the mine system and the geothermal system as the most influential factor. Other important parameters include the injection rate, injection temperature, well spacing, coefficient of thermal

* Corresponding author at: Department of Geology, Ghent University, Ghent, Belgium.
E-mail address: le.zhang@ugent.be (L. Zhang).

https://doi.org/10.1016/j.apenergy.2024.124531
Received 13 May 2024; Received in revised form 8 August 2024; Accepted 16 September 2024
Available online 26 September 2024

expansion, permeability, Young's modulus, and heat capacity. Finally, we propose a DGSA-based optimization framework that accounts for subsurface uncertainty and validate the optimized results. Our results indicate that, with favorable geological conditions, a rational selection of system design parameters can enhance geothermal energy production while ensuring rapid mine cooling and stability. This study provides essential insights for the optimization of deep mine geothermal systems and supports effective decision-making.

1. Introduction

The increasing demand for alternative energy and mineral resources, coupled with the depletion of shallow resources, is driving resource extraction to larger depth. Geothermal energy, abundant beneath the Earth's surface, plays a significant role in providing green, clean, and sustainable energy supplies [1,2]. However, exploiting deep geothermal energy poses challenges due to insufficient subsurface knowledge and substantial upfront exploration costs. Operational mines at depths exceeding 1 km often have temperatures suitable for meaningful heat production and relatively well-characterized geological settings [3]. Therefore, utilizing the existing infrastructure of deep mines for geothermal energy in a safe and efficient manner is critical [4]. Information from subsurface characterization in existing mines can serve as a reference for geothermal extraction, and existing shafts and drifts in mine systems can significantly reduce geothermal drilling costs. Additionally, injecting cold water during geothermal operations cools mining areas through heat exchange, aiding in heat hazard management [5].

Geothermal energy in deep mines is currently pursued through two main approaches: utilizing abandoned mines and the co-extraction of geothermal and mineral resources [6]. In the first approach, abandoned mines, typically flooded after closure, can use the floodwater as an energy medium for geothermal power. Success stories of this method include projects in Germany, the Netherlands, Norway, Spain, the UK, and the USA, where geothermal systems generally operate below 200 m depth with reservoir water temperatures between 10 and 25 °C, providing heat to nearby buildings [7–12]. The second approach, co-extraction, is less common but has seen significant progress in China, where coal mines such as Jiahe, Sanhejian, and Zhangshuanglou, with temperatures exceeding 30 °C, have successfully integrated geothermal extraction. Geothermal energy extraction has proven to be able to reduce the temperature of drifts by 4–6 °C, thereby mitigating heat hazards [13,14]. However, the primary goal of these projects remains mineral extraction, with geothermal production mainly aimed at heat hazard management, resulting in limited use of geothermal energy.

Direct extraction of geothermal energy from bedrock in deep mines, although not yet practiced, is a promising approach. Conceptual models for direct geothermal extraction within deep mines have been proposed and serve as a basis for investigating the system's cooling and heating effects via numerical simulations [15,16]. However, research gaps remain regarding the system stability. Deep mine environments and geothermal systems at depths of several kilometers experience elevated temperatures (typically over 40 °C), high water pressure (typically over 10 MPa), and high geostress (typically over 30 MPa). Injecting cold fluids can significantly disrupt the original stress field, compromising structural safety and stability [17–19]. Stress disturbances in reservoir rocks arise from thermal stress due to temperature changes and poroelastic stress from pore pressure fluctuations. Effective stress reduction due to these factors can jeopardize the stability of surrounding rock [20]. Therefore, coupled thermal–hydraulic–mechanical (THM) studies are essential to ensure efficient geothermal production and cooling while maintaining the mine system safety and stability.

The development of a reliable THM model requires the consideration of various hydraulic, thermal, and mechanical properties. Complex interactions between physical processes, influenced by numerous parameters, make this a time-intensive endeavor. Despite advances in numerical modeling and high-performance computing, the development of reliable THM models remains challenging [21]. Uncertainties arise from incomplete parameter knowledge and the complexity of the subsurface structure [22]. Two main technical aspects contribute to this uncertainty, namely subsurface characterization and development options [23]. Understanding the target reservoir, based on data interpretation and empirical correlations, may not fully capture the subsurface properties, leaving uncertainties [24]. Geothermal system design also influences reservoir responses, with factors like well spacing, injection rate, and temperature being critical considerations [25]. This study also examines the proximity between the geothermal and mine systems in deep mine geothermal models.

Improving the reliability of geothermal systems requires rational parameter selection based on uncertainty analysis. As complex dynamic systems, geothermal systems should be characterized in both space and time [26]. Some studies use local sensitivity analysis to explore how different parameters affect production temperature and stability under THM conditions. Parameters such as Young's modulus, thermal conductivity, heat capacity, and permeability, along with design elements such as injection rate, temperature, and well spacing, significantly influence the system response [27–30]. However, local sensitivity analysis methods, which use partial derivatives or sensitivity coefficients, have limitations. For example, the one-at-a-time sensitivity analysis approach involves changing one parameter at a time while holding other parameters constant to determine their effects. This method provides valuable insights near a baseline point but may not capture the full range of interactions between parameters or model behavior across the entire input space [31]. Global sensitivity analysis, which encompasses the full range of input parameters, is better suited to explore nonlinearities and interactions between parameters [32]. Therefore, the use of global sensitivity analysis is preferable for optimizing complex deep geothermal systems [33]. This method involves generating numerous samples within the probability distribution of the model parameters, simulating system responses, and evaluating their effects. Global sensitivity analysis in geothermal systems has been used to evaluate production temperature, operational efficiency, and system lifespan [34–36]. However, studies on the mechanical stability of co-mining systems are lacking.

This work aims to assess the temperature and stability of deep mine geothermal systems and optimize their design by quantifying the sensitivity of various parameters. Our first contribution is to evaluate the effects of geothermal system operation on mine temperature and stability through numerical simulations. Our second contribution is to quantify parameter sensitivity using DGSA, outlining a framework for system optimization under subsurface uncertainty, and guiding effective decision-making for enhanced geothermal energy production, mine cooling, and stability. The paper is structured as follows: Section 2 outlines the methodology, detailing the THM modeling approach and DGSA used. Section 3 presents the results of THM modeling and uncertainty quantification, highlighting parameter sensitivity and providing recommendations for system optimization. Section 4 discusses study limitations and future research recommendations. Finally, Section 5 concludes by summarizing the main findings.

2. Methodology

A 2D thermo-hydro-mechanical finite element model of a synthetic geothermal system situated directly beneath an existing mine is developed (Fig. 1), implemented in COMSOL Multiphysics. During the operation of the geothermal system, we analyze the evolution of the temperature and stability of the mine system drifts, as well as the evolution of the production temperature of the geothermal system. Subsequently, the responses of temperature and stability generated from 1000 stochastic simulations are used as inputs for DGSA.

Nomenclature

α_T	Coefficient of thermal expansion ([1/K])
$\boldsymbol{\varepsilon}$	Strain tensor
$\boldsymbol{\varepsilon}_{\text{th}}$	Thermal strain tensor
$\boldsymbol{\sigma}$	Total stress tensor
$\boldsymbol{\sigma}'$	Effective stress tensor
λ_{eq}	Equivalent thermal conductivity of porous media ([W/(m K)])
λ_{f}	Thermal conductivity of fluid phase ([W/(m K)])
λ_{s}	Thermal conductivity of solid phase ([W/(m K)])
μ	Fluid dynamic viscosity ([Pa s])
ν	Poisson's ratio
ρ	Density of porous material ([kg/m^3])
ρ_{f}	Density of pore fluid ([kg/m^3])
ρ_{s}	Density of solid phase ([kg/m^3])
ϕ_{mob}	Mobilized friction angle
χ_{f}	Fluid compressibility ([1/Pa])
C_{f}	Heat capacity of fluid phase ([J/(kg K)])
C_{s}	Heat capacity of solid phase ([J/(kg K)])
E	Young's modulus ([Pa])
$F(X)$	Cumulative distribution function of the entire dataset
$F(X\|c)$	Cumulative distribution function of the dataset conditioned on cluster c
k	Permeability ([m^2])
p	Pressure ([Pa])
Q_f	External source or sink of fluid ([kg/(m^3 s)])
Q_T	Heat source term ([W/m^3])
$S(X)$	Sensitivity
$S(X_i\|X_j)$	Second-order conditional effect
t	Time ([s])
T	Temperature ([K])
T_{ref}	Reference temperature ([K])
$\mathbf{C}$	Material's elastic matrix
$\mathbf{g}$	Gravity vector ([m/s^2])
$\mathbf{I}$	Unit tensor
$\mathbf{q}$	Heat flux ([W/m^2])
$\mathbf{u}$	Advective fluid flux ([m/s])
φ	Porosity
τ	Shear stress ([Pa])
σ_n'	Effective normal stress ([Pa])
BEL	Bayesian Evidential Learning
CDF	Cumulative Distribution Function
DGSA	Distance-based Generalized Sensitivity Analysis
LHS	Latin Hypercube Sampling
PDF	Probability Density Function
THM	Thermo-Hydro-Mechanical
VL	Vertical Line between the Injection Well and the Drift Lower Edge

2.1. Governing equations

The theoretical framework is composed of three balance equations, namely the liquid mass balance, the energy balance, and the balance of momentum (or stress equilibrium) equations.

The fluid mass balance equation is written as [37]:

$$\rho_{\text{f}}\left(\varphi\chi_{\text{f}}+\frac{\partial\varphi}{\partial p}\right)\frac{\partial p}{\partial t}+\nabla\cdot(\rho_{\text{f}}\mathbf{u})=Q_f \tag{1}$$

where ρ_{f} [kg/m^3] is the density of the pore fluid, φ is the porosity, χ_{f} [1/Pa] is the fluid compressibility, p [Pa] is the fluid pressure, t [s] is time, $\mathbf{u}$ [m/s] is the advective fluid flux, and Q_{f} [kg/m^3 s] represents an external source or sink.

The fluid flux is given by Darcy's law [38]:

$$\mathbf{u}=-\frac{k}{\mu}(\nabla p+\rho\mathbf{g}) \tag{2}$$

where k [m^2] is the permeability, μ [Pa s] is the fluid dynamic viscosity, and $\mathbf{g}$ [m/s^2] is the gravity vector.

The energy balance equation is given by [38]:

$$\left[(1-\varphi)\rho_{\text{s}}C_{\text{s}}+\varphi\rho_{\text{f}}C_{\text{f}}\right]\frac{\partial T}{\partial t}+\rho_{\text{f}}C_{\text{f}}\mathbf{u}\cdot\nabla T+\nabla\cdot\mathbf{q}=Q_T \tag{3}$$

where ρ_{s} [kg/m^3] and C_{s} [J/(kg K)] are the density and heat capacity of the solid phase, and ρ_{f} [kg/m^3] and C_{f} [J/(kg K)] are the density and heat capacity of the fluid phase, respectively, T [K] is temperature, and Q_T [W/m^3] is the heat source term. $\mathbf{q}$ [W/m^2] is the heat flux given by Fourier's law [38]:

$$\mathbf{q}=-\lambda_{\text{eq}}\nabla T \tag{4}$$

where λ_{eq} [W/m K] is the equivalent thermal conductivity of the porous media material, calculated as [38]:

$$\lambda_{\text{eq}}=(1-\varphi)\lambda_{\text{s}}+\varphi\lambda_{\text{f}} \tag{5}$$

where λ_{s} [W/m K] and λ_{f} [W/m K] are the thermal conductivities of the solid and fluid phases.

The stress equilibrium equation is given by [38]:

$$\nabla\cdot\boldsymbol{\sigma}+\rho\mathbf{g}=\mathbf{0} \tag{6}$$

where $\boldsymbol{\sigma}$ is the total stress tensor and ρ [kg/m^3] is the density of the porous material. The constitutive behavior of the continuum porous medium is formulated in terms of the effective stress tensor $\boldsymbol{\sigma}'=\boldsymbol{\sigma}-p\boldsymbol{I}$ and its conjugate strain tensor $\boldsymbol{\varepsilon}$. The material is assumed isotropic and linear elastic. A general form of the mechanical law is given by [38]:

$$\boldsymbol{\sigma}=\mathbf{C}(\boldsymbol{\varepsilon}-\boldsymbol{\varepsilon}_{\text{th}})+p\mathbf{I} \tag{7}$$

where $\mathbf{C}$ represents the material's elastic matrix (with Young's modulus E [Pa] and Poisson's ratio ν as parameters), and $\mathbf{I}$ is a unit tensor. The thermal strain ε_{th} is expressed as [38]:

$$\boldsymbol{\varepsilon_{th}}=\alpha_T(T-T_{ref})\mathbf{I} \tag{8}$$

where α_T [1/K] is the coefficient of thermal expansion and T_{ref} [K] is a reference temperature.

Finally, water properties are assumed to vary with temperature. The impact of temperature on the dynamic viscosity μ [Pa s], thermal conductivity λ_{f} [W/(m K)], density ρ_{f} [kg/m^3], and heat capacity C_{f} [J/(kg K)] is expressed through the following empirical relations [38]:

$$\mu=1.38-0.028T+1.36\times10^{-4}T^2-4.64\times10^{-7}T^3+8.9\times10^{-10}T^4 \tag{9}$$

$$\lambda_{\text{f}}=-0.869+0.0097T-1.58\times10^{-5}T^2+7.98\times10^{-9}T^3 \tag{10}$$

$$\rho_{\text{f}}=838.47+1.47T-0.0037T^2+3.72\times10^{-7}T^3 \tag{11}$$

$$C_{\text{f}}=12010.15-80.41T+0.317T^2-5.38\times10^{-4}T^3+3.62\times10^{-7}T^4 \tag{12}$$

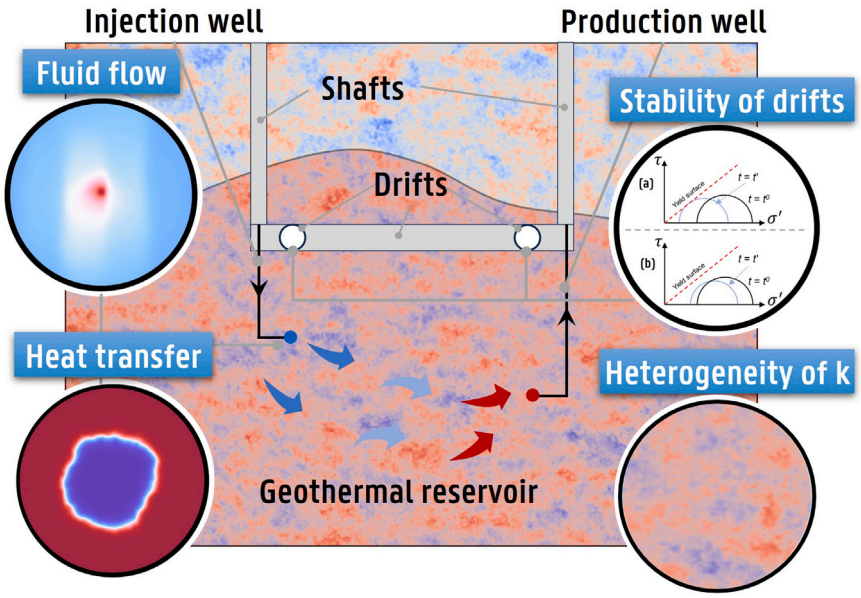

Fig. 1. Conceptual representation of geothermal extraction in a deep mine. Top left: fluid flow around the injection well. Bottom left: heat transfer around the injection well. Upper right: the stability evolution of the mining drifts, represented by Mohr–Coulomb circles (a) indicating failure, (b) indicating stability. Lower right: heterogeneity of the permeability field.

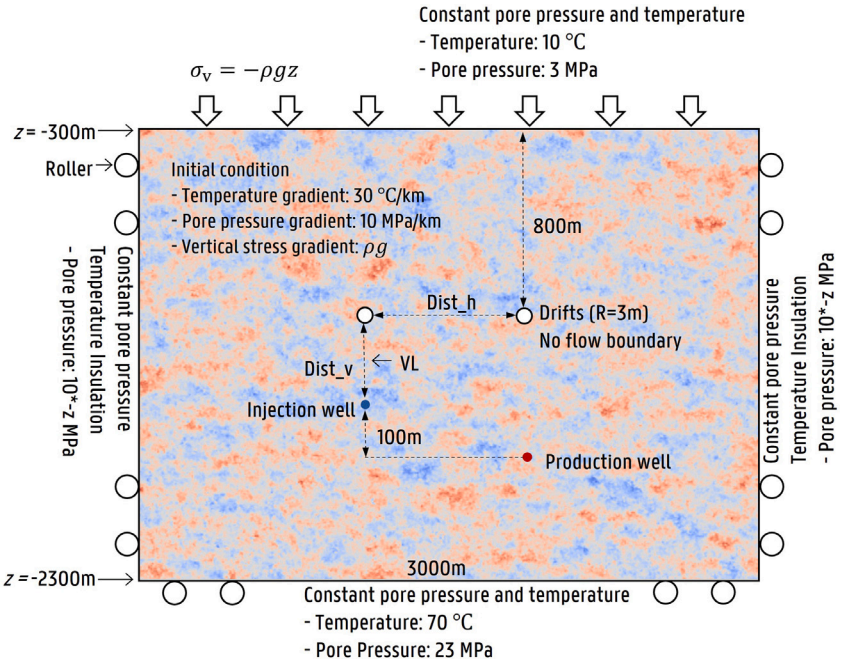

Fig. 2. Schematic of heterogeneous 2-D numerical model including initial and boundary conditions (not to scale). In the isothermal injection scenario in Section 2 and model scenarios in Section 3, the initial condition of temperature is set to 30 °C, with both the top and bottom temperatures at 30 °C, disregarding the temperature gradient.

2.2. Geometry, initial and boundary conditions and model parameters

We develop a 2-dimensional conceptual model of a geothermal system, as depicted in Fig. 2. The model includes two mine drifts, each with a radius of 3 m, located at a depth of 1100 m and spaced 500 m apart. The geothermal injection and production wells are located below the two drifts, at vertical distances of 120 m and 220 m, respectively, from the mine drifts. The model domain is 3000 m wide, centered on the midpoint between the two drifts, with a depth range from 300 m to 2300 m.

The surface temperature is set to 10 °C and the geothermal gradient to 30 °C/km. The sides of the domain are considered as thermally insulated. The pressure boundary condition represents an initial hydrostatic gradient of 10 MPa/km, with the top boundary set at 3 MPa and the bottom one at 23 MPa. No-flow boundary conditions are considered on the sides. Vertical self-weight stress is applied to the top, and roller support conditions are employed on the remaining three sides. Gravity influences both pressure and effective stress within the model, and stress equilibrium is established prior to the operation of the geothermal system.

Comparing isothermal and non-isothermal injection is a typical approach for analyzing thermal stress effects in THM models [39]. In this work, to accurately study the impact of thermal stress and poroelastic stress on the system, we establish two scenarios: (i) isothermal injection

Table 1
Geological and design parameters and material properties used in the numerical model.

Type	Parameters	Unit	Iso/Non-Iso simulations	Stochastic simulations	Abbreviation
Heterogeneity parameters	Range [33,40]	m	100	U[20 200]	Range
	Orientation [35]	°	60	U[60 120]	Angle
Design parameters	Well spacing [41]	m	500	U[200 800]	Dist_h
	Vertical distance from the drift to the well	m	120	U[50 200]	Dist_v
	Temperature of injected water [29]	°C	10, 30	U[10 30]	T_inj
	Pumping rate [41]	kg/s	50	U[20 70]	P_rate
Material properties	Mean of $\log_{10} k$ [42]	m^2	−13	U[−14 −12]	K_mean
	Variance of $\log_{10} k$ [35]	m^2	0.5	U[0.1 1]	K_var
	Porosity [24]	1	0.125	U[0.05 0.2]	Porosity
	Young's modulus [42]	GPa	15	U[10 20]	Y_modu
	Density [30]	kg/m^3	2500	U[2300 2700]	Dens
	Thermal expansion [29]	1/K	5e−6	U[1e−6 1e−5]	T_expa
	Heat capacity [29]	J/kg K	1050	U[800 1300]	H_capa
	Thermal conductivity [30]	W/m K	1.85	U[1.2 2.5]	T_cond
	Poisson's ratio [37]	1	0.25	0.25	/
	Biot's coefficient [37]	1	1	1	/

(with both domain and injected water temperature of 30 °C and (ii) non-isothermal injection (with an injected water temperature of 10 °C and domain temperature following the geothermal gradient).

To consider spatial heterogeneity, we generate permeability, porosity, and Young's modulus fields through sequential Gaussian simulation, with a range of 100 m for the variogram in the flow direction and a primary direction set at 60° from the horizontal [35,40]. The triangular mesh used in this study contains about 24,000 elements in each model. The parameters of the system and material properties utilized in the simulation are summarized in Table 1.

2.3. Mine stability assessment

The mobilized friction angle ϕ_{mob} is used to assess the stability of the rock mass. Assuming a Mohr–Coulomb failure criterion, the mobilized friction angle is given by [39]:

$$\phi_{mob} = \tan^{-1}\left(\frac{\tau}{\sigma_n'}\right) \tag{13}$$

where τ [Pa] is the shear stress and σ_n' [Pa] is the effective normal stress. Assuming a friction angle of 30°, a point of the rock mass is deemed stable when ϕ_{mob} is lower than 30°.

2.4. Stochastic analysis

Uncertainties in our THM model development stem from subsurface heterogeneity and design parameters. The spatial variability of geological formations and limited data introduces significant uncertainty affecting the material parameters. On the other hand, operational and design parameters, such as injection rates, temperatures, and well spacing, are adjustable parameters.

To address these uncertainties, we employ the Latin Hypercube Sampling (LHS) method. LHS is a statistical technique used to generate a distribution of plausible collections of parameter values from a multidimensional distribution [43]. This method is chosen for its efficiency in sampling the parameter space, ensuring systematic exploration of each parameter's entire range. Except for the fixed Poisson's ratio of 0.2 and Biot's coefficient of 1, we assign uniform distributions to 14 critical parameters, including 4 design parameters, 8 material properties, and 2 heterogeneity parameters, as detailed in Table 1. The uniform distribution assumption reflects our limited prior knowledge, providing an unbiased approach to exploring the parameter space. The range of these parameters is derived from existing literature, with some ranges broadened to encompass extreme scenarios. Using LHS, we generate 1000 realizations of the model parameters. This sample size balances computational feasibility with the need for comprehensive uncertainty exploration, as further detailed in the discussion section. Each realization represents a potential scenario of subsurface and operational conditions. The generated parameter sets are used to conduct a series of parallel forward simulations. These simulations capture a wide range of potential outcomes under different uncertainty scenarios.

2.5. Distance-based generalized sensitivity analysis

This work employs Distance-based Generalized Sensitivity Analysis (DGSA) to analyze the sensitivity of the selected model parameters to the reservoir response simulated by the stochastic simulation [32,33]. DGSA is capable of handling single outputs, as well as more complex time-dependent or spatio-temporal outputs [44]. A distinctive feature of DGSA is its use of clustering algorithms to categorize output variables into different groups based on their mutual distances, thereby facilitating the assessment of uncertainty.

Initially, this method divides outputs into several clusters using a distance-based clustering approach, examining the cumulative distribution function (CDF) of a specific parameter in each cluster and comparing it to the original distribution. This process yields the normalized sensitivity index by considering the average differences between the CDFs in each cluster. DGSA employs a resampling technique to quantify variations among samples redistributed within clusters. Sensitivity S is represented by the average of the mean differences across all categories:

$$S(X) = \frac{1}{C}\sum_{c=1}^{C} \hat{d}_{c,s}, \text{ with } \frac{\hat{d}_c}{\check{d}_a^c} \tag{14}$$

$$\hat{d}_{c,i} = d_{L1}F(X), F(X|c), c = 1, \ldots, C \tag{15}$$

where $\hat{d}_{c,s}$ is the normalized distance within a cluster, $\hat{d}_c$ is the average of the distances for cluster c, and $\check{d}_a^c$ is the a_{th} quartile of the distances within cluster c, with a being set to 0.95, and $\hat{d}_{c,i}$ is the $L1$ distance between the cumulative distribution function of the entire dataset $F(X)$ and the cumulative distribution function of the dataset conditioned on cluster c, $F(X|c)$. If distributions within various categories differ significantly, the parameter is deemed sensitive. In this study, parameters are defined as sensitive if their sensitivity value exceeds 1 [45].

In similar context, it is possible to determine a conditional effect (i.e. interaction between parameters). This approach delineates the impact of one parameter when it is conditioned upon the level (or grouping) of a different parameter. The method for deriving the second-order conditional effect adheres to a methodology comparable to the previous one, expressed as follows [45]:

$$S(X_i|X_j) = \frac{1}{C}\frac{1}{L}\sum_{c=1}^{C}\sum_{l=1}^{L} \hat{d}_{c,i|j}, l^S \text{ with } \hat{d}_{c,i|j}, l^S = \frac{\hat{d}_{c,i|j,l}}{\hat{\hat{d}}_{c,i|j,l}(a)}, \tag{16}$$

$$i, j = 1, \ldots, k; l = 1, \ldots, L; c = 1, \ldots, C$$

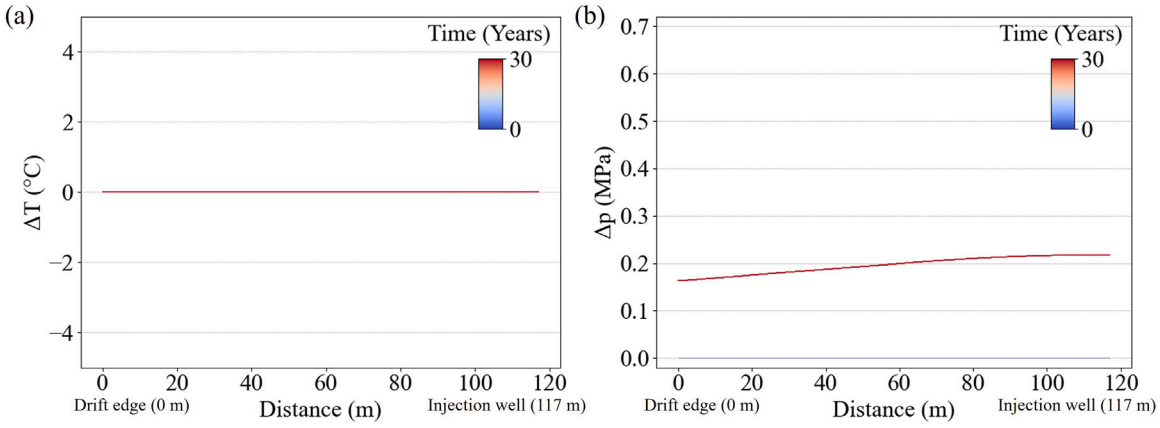

Fig. 3. Spatiotemporal evolution of ΔT and Δp on the measurement line VL during isothermal injection: (a) ΔT, (b) Δp.

Here, the term $\hat{d}_{c,i|j,l}$ is the normalized $L1$ norm distance that accounts for the disparity between the distribution of X_i in class C and the distribution where X_j is at a specific level l.

In this study, the number of clusters is preset to 3, categorizing responses into "good", "moderate", and "poor" to assess the model's performance. As an unsupervised method, the clustering approach involves defining response labels based on a subjective interpretation of the expected response. Smaller changes in stability are considered "good" when evaluating the stability of drifts, while faster cooling is considered "good" for the temperature of drifts. The DGSA method contributes to parameter optimization in the model in two ways. First, by analyzing the distribution of the CDFs of the sensitive parameters across the 3 groups to inform model design, aiming to align sensitive parameters' probabilities with the "good" label. Second, by fixing values of insensitive parameters at the average of the initial value range, which reduces the uncertainty of the system responses and assists in model calibration and optimization.

3. Results

3.1. Thermo-hydro-mechanical modeling

Simulations of 30-years geothermal operation and associated geomechanical reservoir response are conducted for both isothermal injection (30 °C) and non-isothermal injection (10 °C), with the latter temperature being below the initial in-situ temperature. This study focuses on the effects of the injection well on the left drift, particularly along the vertical line (VL) between the injection well and the drift's lower edge.

3.1.1. Coupling between fluid pressure and temperature

Figs. 3 and 4 present the evolutions of the change in temperature and pore pressure between the drift edge and injection well with time for the isothermal and non-isothermal simulations. As illustrated in Fig. 3, under isothermal injection conditions, the temperature along the VL remains constant, and the pressure change stabilizes within a very short time (0.1 years), with greater pressure values closer to the injection well. In the thermo-hydro-mechanical model, pressure changes migrate rapidly, with more pronounced pressure changes around the injection well that gradually diffuse towards the drift edge (Fig. 4). Conversely, the area of temperature disturbance expands more slowly. The maximum temperature drop (−20 °C) is controlled by the injection temperature. The decrease in temperature caused by the propagation of the cold front leads to a notable increase in pressure. After 30 years of operation the change in pressure Δp near the injection well caused by isothermal injection approximates 0.22 MPa, while after non-isothermal injection, it reaches 0.75 MPa. In the region near the drift, the pressure change rises from 0.16 MPa to 0.21 MPa, marking a 31% increase. This occurs because in areas affected by temperature drop, the decrease in fluid temperature leads to an increase in dynamic viscosity, which impedes fluid flow and leads to increased pressure in that area, thus potentially increasing the risk of instability. In non-isothermal injection, the mechanical response is not solely the result of pressure or temperature acting independently, but rather a combined effect. Initially, a rapidly developing pressure front is observed, followed by the thermal effect on cooling areas, and the pressure changes in these cooling areas during the process.

3.1.2. Evolution of the poroelastic and thermal stress fields

The response characteristics of poroelastic stress and thermal stress reflect those of pressure and temperature migration, both adversely affecting the stability of the rock. An increase in pore pressure reduces the effective stress in the rock, leading to an increase in the mobilized friction angle, denoted as an increase in ϕ, and a heightened likelihood of rock failure. Injection of cold water decreases thermal stress in the rock, increasing the risk of failure in the surrounding rock and weakening the stability of the mine drifts [20].

Due to the excavation, a pronounced stress concentration is observed within approximately 5 radius (15 m) of the drift [46]. At the drift's edge, initial ϕ can reach 80°, with certain areas exhibiting low ϕ due to changes in the maximum and minimum principal stresses (Fig. 5a). A comparison of the impacts of isothermal and non-isothermal injection on ϕ demonstrates that temperature significantly influences system stability more than pressure does and the variation in ϕ values mirrors the characteristics of temperature propagation, as shown in Fig. 5. In the area distant from the drift, as indicated by the dashed line on the right side of Fig. 5(b), ϕ typically ranges from 21° to 26°. However, at the dashed line's left, the initial ϕ values are significantly affected by the excavation. Considering this study is conducted on the foundation of an existing mine system for geothermal operation, we posit that stability on the left side of the dashed line is controlled by excavation, assuming the stress concentration area around the drift remains safe due to support. Conversely, the right side is affected by geothermal operation, and if the ϕ on this side exceeds 30° during geothermal operation, failure is reached. We designate the position 5 radius (15 m) below the drift as a potential risk point for monitoring the mechanical response during system operation. Specifically, in the area between the drift and the injection well, a pattern of ϕ initially decreasing and then increasing suggests that while the surrounding rock's stability is finally weakened, there is an improvement in stability at the early stage.

3.1.3. Evolution of the mine stability at the potential risk points

During simulation of the 30-year geothermal operations, we examine the changes in principal stresses ($\Delta\sigma_1$, $\Delta\sigma_3$), pressure (Δp), mobilized friction angle (ϕ_{mob}), and temperature (T) at the potential risk point (5

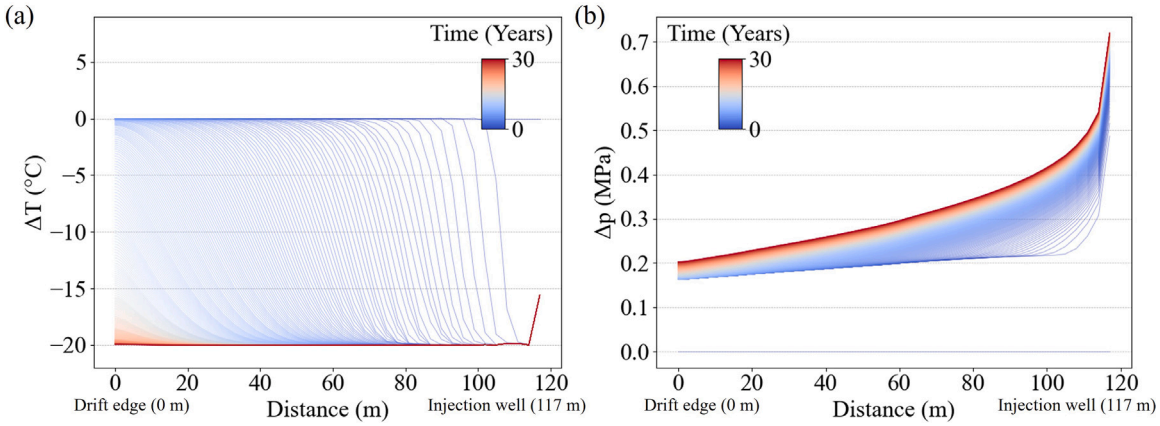

Fig. 4. Spatiotemporal evolution of ΔT and Δp on the measurement line VL during non-isothermal injection: (a) ΔT, (b) Δp.

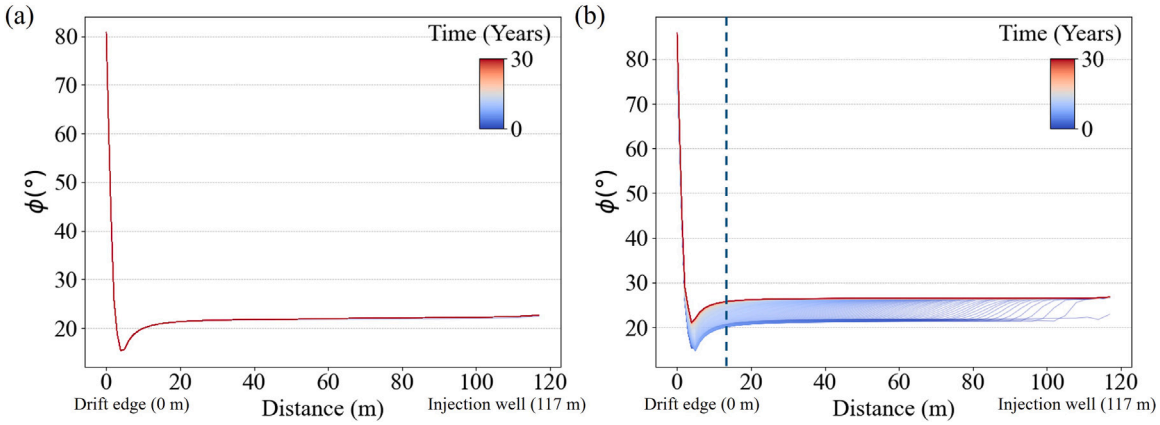

Fig. 5. Spatio-temporal evolution of ϕ on the measurement line VL stability: (a) isothermal injection, (b) non-isothermal injection.

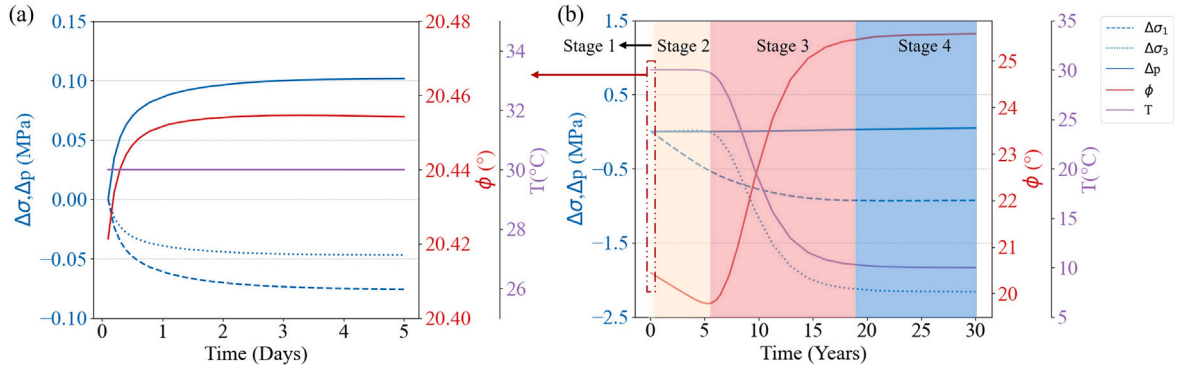

Fig. 6. Effective stress, pressure, mobilized friction angle, and temperature changes at potential risk points: (a) 5-day injection, (b) 30-year injection.

radius (15 m) below the drift) to evaluate the evolution of stability. The changes in stability at the risk point can be divided into four distinct stages (Fig. 6):

1. Slight reduction (0–5 days): Fig. 6(a) reveals that 5 days post-injection, both σ_1 and σ_3 decrease as a result of the rapid migration of injection-induced pressure and an increase in pore pressure. This leads to an increase in the mobilized friction angle, hence a decrease of stability, which is however limited.
2. Minor enhancement (0–6 years): In this phase, the temperature remains relatively constant. Due to the increase in thermal stress around the injection well, the major principal stress σ_1 at the potential risk point decreases, but σ_3 experiences a slight increase due to stress arching. Therefore ϕ_{mob} decreases by about 0.6°, indicating an improvement in stability.
3. Transition (6–19 years): As the temperature of this point begins to decrease, influenced by thermal stress, both σ_1 and σ_3 decrease, indicating significant reduction in the stability.
4. Deterioration (19–30 years): The temperature and mobilized friction angle stabilize, as the area becomes completely encompassed by the spread of the cold plume.

Although the observed behavior provides valuable insights into the processes taking place and can be generalized, it remains characteristic of one set of subsurface properties and design parameters, especially in

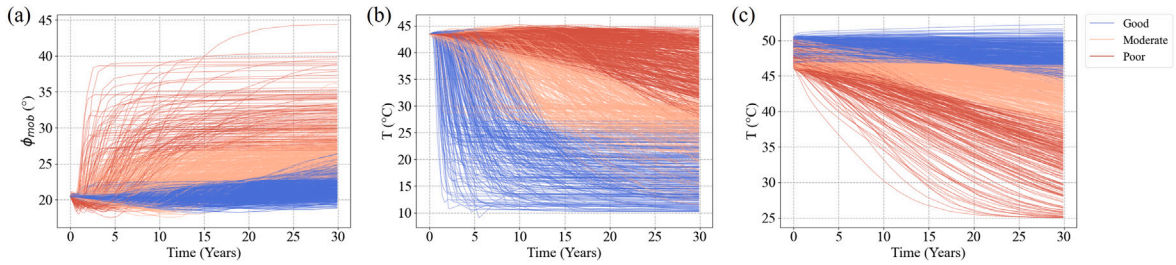

Fig. 7. Clustering results of response: (a) stability of the drift, (b) temperature at the drift, (c) temperature at the production well.

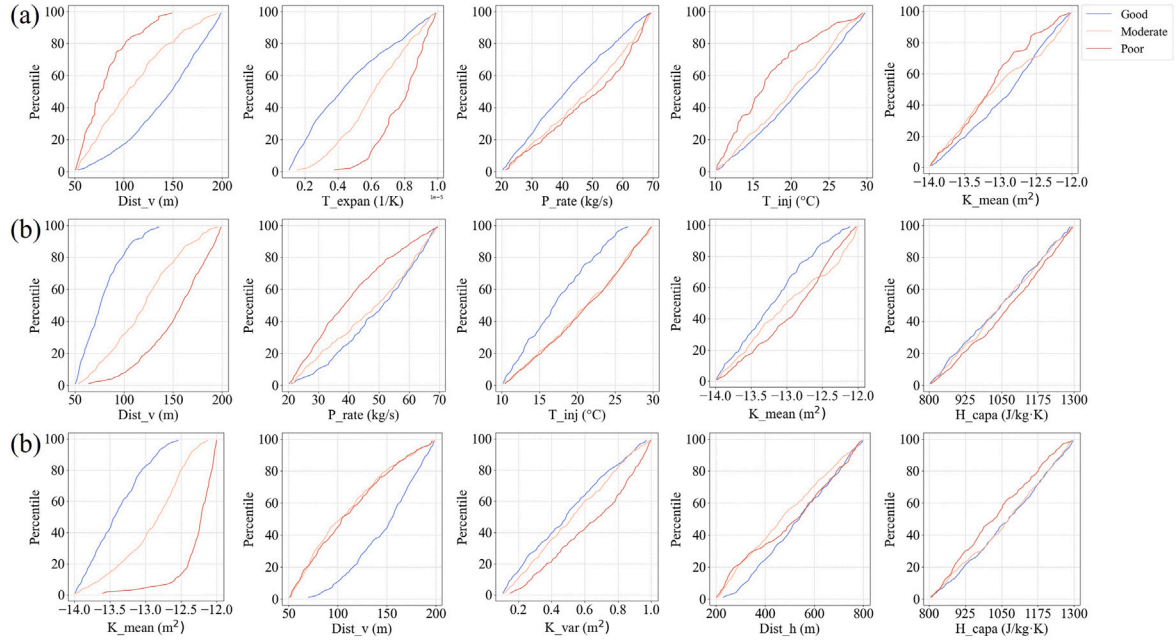

Fig. 8. CDF distribution of top 5 parameters with greatest variance in responses across 3 clustering groups: (a) stability of the drift, (b) temperature at the drift, (c) temperature at the production well.

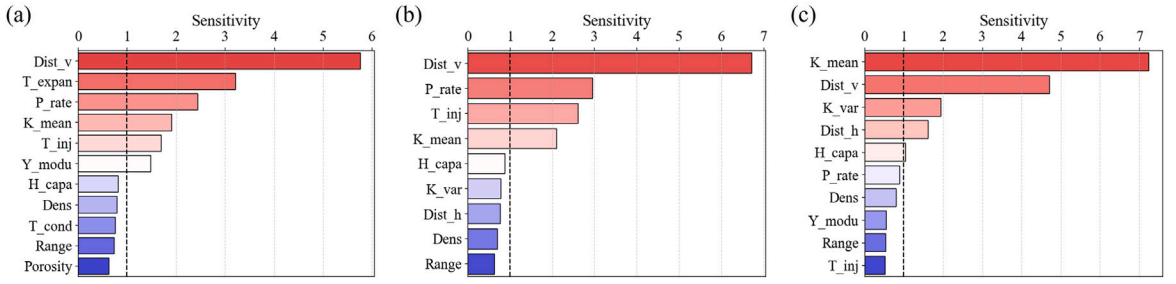

Fig. 9. Sensitivity analysis results of responses, with parameters having a sensitivity value over 1 classified as sensitive (including all sensitive parameters and the top 5 insensitive parameters): (a) stability of the drift, (b) temperature at the drift, (c) temperature at the production well.

terms of absolute values. Therefore, it is crucial to consider all potential risks more systematically and quantitatively.

3.2. Uncertainty quantification and design optimization

3.2.1. Sensitivity analysis

As previously mentioned, 3 clusters were defined in this study, categorizing responses into 'good', 'moderate', and 'poor' clusters using the K-medoids clustering [33]. Fig. 7 displays the clustering results of the 1000 realizations. For the drift stability, the group with small ϕ values is categorized as "good" (blue). For the temperature at the drift, the group exhibiting fast temperature drop is deemed "good". Whereas for the production well temperature, the group with slow temperature decrease is classified as "good". Fig. 8 illustrates the CDF distributions of the 5 parameters showing the most significant distribution differences across the responses. Based on Fig. 8, the sensitivity of each parameter across the 3 groups is quantified, Specifically, DGSA employs a resampling technique to quantify variations among samples redistributed within clusters. Sensitivity is represented by the average of the mean differences across all categories, if distributions within various categories differ significantly, the parameter is deemed sensitive, defining parameters with a sensitivity value over 1 as sensitive [33].

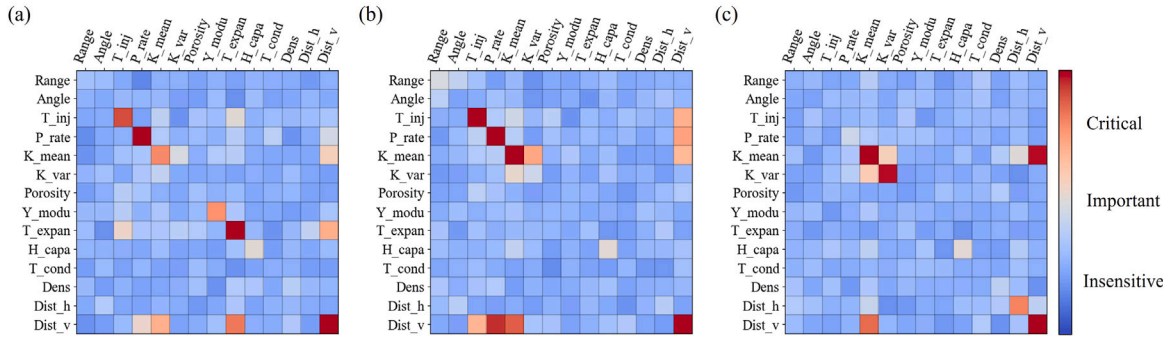

Fig. 10. Outcomes of inter-parameter sensitivity values: (a) stability of the drift, (b) temperature at the drift, (c) temperature at the production well.

Fig. 9(a) identifies the vertical distance between the injection well and the drift as the most sensitive parameter to the stability of drift, followed by the thermal expansion coefficient, pumping rate, permeability, and injection temperature. An increased vertical distance correlates with enhanced safety of the drift, as shown in Fig. 8(a). This is because a greater vertical distance reduces the thermal and mechanical impact of the injected cold water on the drift, thereby enhancing its stability. In the "poor" category, about 78% of the realizations feature a vertical distance of less than 100 m. The remaining 22% are located at 100–150 m, whereas in the "good" category, 83% of the realizations have a vertical distance exceeding 100 m. Notably, when the distance exceeds 150 m, samples categorized as "poor" no longer appear. The higher sensitivity of the thermal expansion coefficient compared to permeability and injection rate indicates that thermal stress more significantly impacts the stability of the drift than poroelastic stress. Fig. 8(a) shows that a higher thermal expansion coefficient is associated with an increased risk. In the "poor" category, most realizations display high ϕ values towards the end of the simulation. However, the influence of poroelastic stress cannot be ignored. A higher thermal expansion coefficient increases the risk of instability by amplifying the stress changes induced by temperature variations. Similarly, higher injection rates and lower injection temperatures lead to larger pressure and temperature gradients, adversely affecting stability.

For the drift temperature as shown in Fig. 9(b), the vertical distance between the drift and the well is the primary parameter affecting cooling efficiency. A smaller vertical distance results in more effective cooling as the drift is closer to the cold source. Additionally, permeability and injection rate are key parameters influencing heat transfer, with higher permeability and injection rates leading to more rapid cooling. This suggests that optimizing these design parameters can significantly enhance the cooling efficiency of the geothermal system.

In Fig. 9(c), the sensitivity analysis for the production well temperature identifies permeability as the most sensitive parameter, higher permeability facilitates quicker thermal breakthrough, reducing production temperature, which can be defined as a 10% decrease in the difference between the initial production temperature and the injection temperature. Additionally, both the vertical distance between the well and the drift and the well spacing are sensitive, particularly the vertical distance. In this model, a greater vertical distance indicates increased depth, consistent with the conventional notion that deeper geothermal systems are more efficient [47]. Smaller well spacing increases the likelihood of thermal breakthrough, but this effect was not pronounced within the 30-year simulation period. It is anticipated that with extended extraction duration or high rates, the sensitivity of well spacing to production temperature will increase.

Fig. 10 delves into the inter-parameter sensitivity, revealing complex interactions among the system's parameters. For drift stability, the interaction between vertical distance and thermal expansion is particularly significant, reinforcing the importance of thermal stress management. The temperature responses at the drift and production well show notable interactions between permeability, injection rate, and well spacing, indicating their combined influence on thermal propagation and system performance. These interactions emphasize the need for a holistic approach in parameter optimization, considering combined effects rather than isolated impacts.

In summary, vertical distance and permeability emerge as the most sensitive parameters among the three responses, each showing diverse distribution trends in the "good" category. Crucial design parameters of the model, including pumping rate, injection temperature, and well spacing, as well as some material properties, such as permeability, thermal expansion coefficient, Young's modulus, and heat capacity, prove particularly sensitive. Other material properties, such as porosity, thermal conductivity, density, range, and angle, do not show significant sensitivity in the responses or interactions. Therefore, maintaining these five parameters at the average of their prior value ranges is reasonable. By reducing the model's complexity and uncertainty via the DGSA method, we can utilize the results to refine and limit the range of sensitive parameters, enhancing the probability of achieving desired performance of the system.

3.2.2. *Suggestions to decision-making*

This section introduces a DGSA-based optimization framework, which involves determining a parameter range by evaluating the probability density functions (PDF) of sensitive parameters, thereby enhancing the likelihood of achieving responses categorized as "good" during the DGSA clustering in forward simulations.

For parameters that appear only once across the sensitivity analyses, a single probability density is evaluated. For parameters appearing multiple times, a statistical overlap analysis method is employed, identifying common areas between different groups by analyzing the overlap of probability densities, akin to the concept of Pareto optimality. A range is defined that effectively balances the probability distributions among each group. By setting a threshold of 90% of the peak value on the overlap probability density, the optimal parameter value range is calculated. A range exceeding this threshold indicates a high likelihood of the parameter satisfying the criteria in one or all groups, thus representing the optimal parameter distribution range.

Using the vertical distance as an example (see Fig. 11), this parameter shows varying distribution trends in the "good" category for different responses. For stability of the drift and temperature at the production well, larger values are favored, with the most concentrated distribution observed at 180 m. Conversely, for cooling of the drift, smaller values are desirable, with approximately 70 m identified as the optimal range for cooling. According to this method, the peak of the probability distribution across the three categories occurs around 112 m, establishing the optimized range as 109 m to 117 m. While this

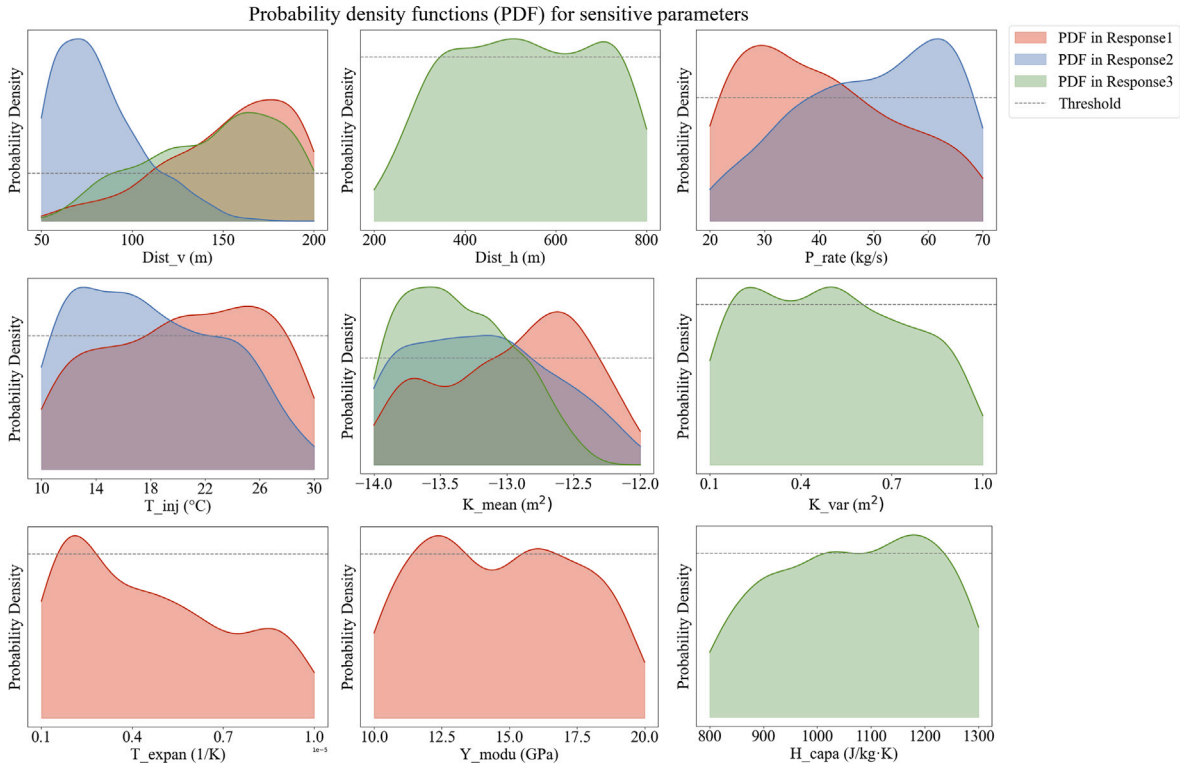

Fig. 11. Parameter optimization process: Red, blue, and green represent the probability density functions for parameters of samples labeled as "good" for stability of the drift (Response1), temperature at the drift (Response2), and temperature at the production well (Response3), respectively.

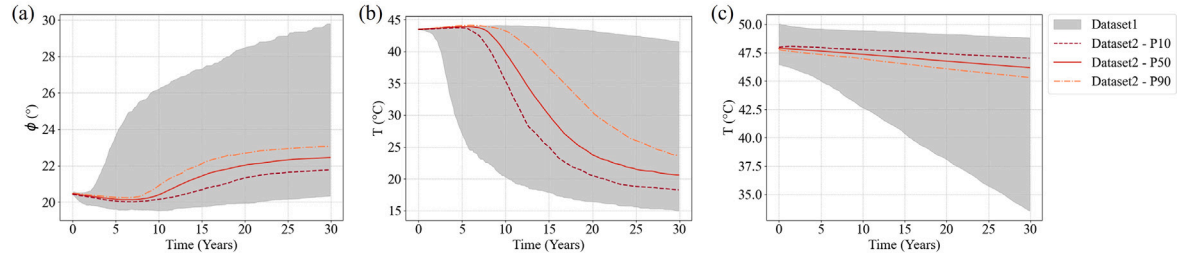

Fig. 12. P10, P90 ranges on dataset1 (before optimization) and P10, P50, P90 curves on dataset2 (after optimization): (a) stability of the drift, (b) temperature at the drift, (c) temperature at the production well.

Table 2
Prior model parameters and optimal value used for verification.

Type	Parameters	Prior values	Suggested values
Design parameters	Well spacing (m)	U[200 800]	U[345 745]
	Vertical distance from the drift to the well (m)	U[50 200]	U[109 117]
	Temperature of injected water (°C)	U[10 30]	U[17 22]
	Pumping rate (kg/s)	U[20 70]	U[38 47]
Material properties	Mean of $log_{10}k$ (m^2)	U[−14 −12]	U[−13.1 −12.8]
	Variance of $log_{10}k$ (m^2)	U[0.1 1]	U[0.16 0.6]
	Young's modulus (GPa)	U[10 20]	U[11.4 16.7]
	Thermal expansion (1/K)	U[1e−6 10e−6]	U[1.5e−6 2.9e−6]
	Heat capacity (J/kg K)	U[800 1300]	U[1015 1235]

method may not always yield the optimal expected response when optimizing parameters with diverse distributions, it effectively mitigates the likelihood of poor-case scenarios in the system response.

The recommendations for optimized sensitive design parameters and favorable material parameters are provided in Table 2. These results demonstrate that the suggested design parameter ranges can significantly enhance the performance of geothermal systems beneath deep mines. This applies particularly to geological layers where the material properties, specifically permeability, Young's modulus, thermal expansion coefficient, and heat capacity, align with those listed in Table 2.

3.2.3. *Verification of the suggestions*

In the preceding section, we determined the optimal design parameters and ranges of material properties for optimal system performance.

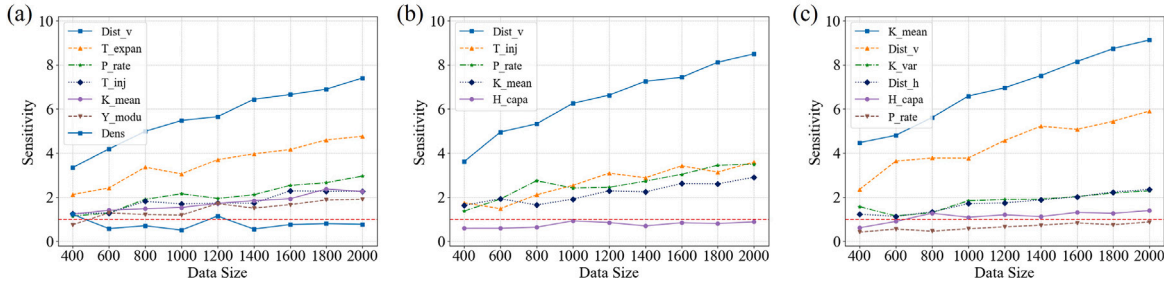

Fig. 13. Impact of sample size on DGSA result analysis: (a) stability of the drift, (b) temperature at the drift, (c) temperature at the production well.

Building on this, we generated 200 new realizations using LHS, sampling from the optimal parameter ranges to validate the feasibility of this approach. For each group of responses, both before and after optimization, we computed the P10, P50, and P90 curves and compared the distribution ranges to validate the optimal parameter selection.

The post-optimization results demonstrate a significant reduction in uncertainty regarding the stability of the drift compared to the initial range. In Fig. 12(a), the maximum ϕ in the P90 curve is 22.8°, compared to 29.6° in the initial range, indicating a considerable improvement in stability and no failure occurring in any realization. The cooling effect of the drift is also optimized, resulting in a more focused distribution. Within approximately 15 years, half of the realizations achieve at least a 13 °C temperature reduction. Although it is not possible to achieve the best outcomes simultaneously for responses with divergent distribution trends, the optimized parameter range effectively avoids poor scenarios where the drift either suffers damage or fails to cool down, making the optimization highly effective.

The temperature at the production well also exhibits a highly desirable distribution. None of the 200 realizations show signs of thermal breakthrough after 30 years of system operation. These observations suggest that the optimization of model parameters is both feasible and effective. Note that since the optimal design parameters were selected based on the full parameter range, we expect to avoid "poor" behavior even for less favorable subsurface parameter combinations, although the risk would increase in such cases.

3.2.4. Sample size of the distance-based generalized sensitivity analysis

The sample size significantly influences the results of the DGSA [35]. To ensure optimal results using the smallest possible sample size, we utilized a 5-fold cross-verification technique, assessing the DGSA results in multiple scenarios with sample sizes ranging from 400 to 2000 (see Fig. 13). Our analysis indicates that for the stability of the drift, when the sample size reaches 600, the least sensitive parameter, Young's modulus, becomes sensitive. With smaller sample sizes, the influence of Young's modulus on the mechanical response might be neglected. Similarly, the heat capacity appears non-sensitive for the temperature of the production well until the sample size increases to 800. This shift further highlights the critical role of sample size in identifying key sensitive parameters. The sensitivity of other parameters remains unchanged across all sample sizes. Furthermore, the hierarchy of parameter sensitivity remains consistent with the outcomes observed in large samples, underscoring the DGSA method's effectiveness even with limited sample sizes. This approach proves adequate for discerning the sensitivity of crucial parameters, as evidenced by our temperature analysis of the drift, wherein all sensitive parameters display sensitivity from the smallest sample size evaluated.

Considering these findings, we recommend an approach for determining the sample size for DGSA analysis. Begin with an initial sample size, increasing in batches of 200 samples, and stop when the sensitivity results stabilize. For this study, this method led us to recommend a sample size of 800, ensuring accurate sensitivity evaluation and reliable analysis outcomes in a computationally efficient manner.

4. Discussion

This study aims to assess the temperature and stability of deep mine geothermal systems and optimize their design by quantifying the sensitivity of various parameters to enhance geothermal energy production, achieve rapid mine cooling, and maintain stability.

In the data generation phase, the selection of sample size is crucial to ensure the reliability and robustness of the datasets. We use Latin Hypercube Sampling (LHS) to generate a dataset that spans the parameter space and verify the reasonableness of the 1000 prior samples from two perspectives. First, it is essential to ensure that the number of samples fully covers the prior uncertainty range and provides a robust uncertainty boundary. We employ LHS to achieve an even distribution of samples across the prior space, thus avoiding duplicate or very similar samples. The uncertainty boundary curves (P10 and P90) do not change significantly between 800 and 1000 samples, indicating that a sample size of 1000 is sufficient to capture the essential uncertainty in the model output (see Fig. 14). Second, the sample size must also be adequate to support reliable sensitivity analysis. We assess the impact of sample size on sensitivity results, as detailed in Section 3.2.4, confirming that the sample size of 1000 is sufficient to derive realistic, stable and reliable sensitivity analysis results for the involved parameters.

After ensuring the samples provide a reliable and comprehensive dataset, we optimize the model design using a DGSA-based optimization method, which is more suitable for our research goals compared to heuristic algorithms such as Genetic Algorithms [48]. While Genetic Algorithms can find a single optimal solution, they are not ideal for broad exploration, especially when model parameters' values and spatial distribution are uncertain. Optimization methods that include uncertainty, as demonstrated in other studies [40,49], are more appropriate for our research. Our focus is on determining the overall behavior and performance range of the geothermal system under different parameter combinations rather than finding a single optimal solution. Given the inherent uncertainty in subsurface parameters in geothermal system design, decision-makers need to understand a range of acceptable parameter values. This broader understanding allows for more informed decision-making, ensuring the system robustness and adaptability. Genetic Algorithms requiring continuous iterative optimization to find the optimal solution significantly increase computational burden, as each iteration requires running a new forward model, limiting the possibility of parallel computation. This is particularly significant in complex geothermal modeling, where computational resource consumption can be enormous. Our DGSA-based optimization requires only 1000 forward model runs, each independent, allowing for complete parallelization if needed. The optimized results are successfully validated with 200 samples generated using the LHS method, with the sample size determined based on the coverage of prior uncertainty, as shown in Fig. 15.

The main limitations of our study are threefold. Firstly, our study utilizes a 2D model, which is not as accurate as a 3D model. A 3D model would provide a more comprehensive and realistic representation of the geothermal system, capturing the complex interactions

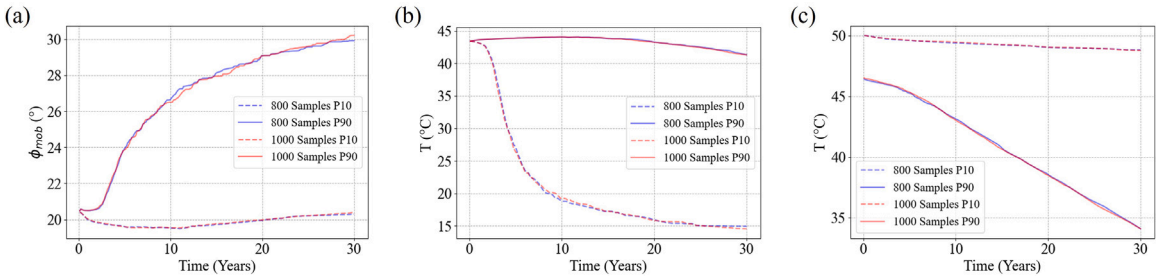

Fig. 14. The uncertainty boundary curves (P10 and P90) of 800 and 1000 samples from prior: (a) stability of the drift, (b) temperature at the drift, (c) temperature at the production well.

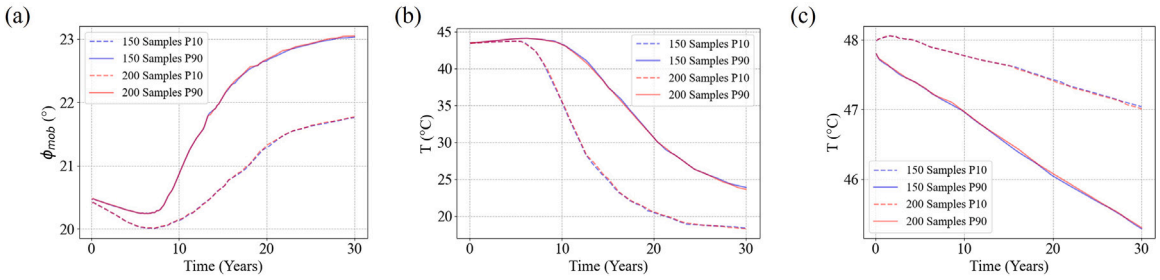

Fig. 15. The uncertainty boundary curves (P10 and P90) of 150 and 200 samples from the optimization: (a) stability of the drift, (b) temperature at the drift, (c) temperature at the production well.

between thermal, hydraulic, and mechanical processes in three dimensions. However, the computation time for a 3D model is significantly larger, particularly for large-scale simulations. Although our computation method allows for parallel processing of samples, the time consumption remains considerable. Considering computational resource limitations, we chose to use a 2D model to reduce computational cost, justified by similar sensitivity patterns expected in both 2D and 3D models. Nevertheless, incorporating more detailed 3D models should be part of future research when computational resources are sufficient.

Secondly, a common limitation in conceptual geothermal system simulation studies is the lack of experimental data and field validation. This means our findings are based solely on numerical simulations, which can affect the accuracy of model predictions in practical scenarios. However, our primary objective is to contribute to the design of systems before actual production data are available, providing preliminary insights and guiding principles for system optimization. This approach lays the groundwork for subsequent experimental validation and field studies, which can refine and improve the model based on real data.

Thirdly, the use of an elastic model in our study cannot adequately represent rock failure and the damage zone. Elastic models assume linear and reversible behavior, failing to capture the yielding and permanent deformation characteristics of rocks over the long-term operation of geothermal systems. However, for the purpose of this study, which focuses on assessing the risk of failure, the elastic model is sufficient. Incorporating plastic models, which account for both elastic and plastic deformations, would provide better predictions of stress distribution and material response over long-term geothermal operations [50,51].

For future research, we plan to validate our findings by obtaining field data for further validation and calibration of our model. Incorporating real-world data will make our research findings more accurate and practically applicable. Additionally, DGSA allows the identification of optimal parameter ranges before performing costly field investigations or investments. The next logical step is to update uncertainty quantification once additional data become available, either from field experiments to better characterize subsurface parameters, effectively reducing the prior range of uncertainty of some subsurface parameters such as permeability and thermal expansion, or from early production data. Bayesian Evidential Learning (BEL) is an effective strategy in such contexts [35]. BEL bypasses complex model inversion or data assimilation by directly predicting target variables from data through machine learning, which is extremely effective for resource-intensive multiphysical coupling response predictions. BEL would therefore be well-suited for application in deep mine stability, as demonstrated in previous research [34,40].

5. Conclusions

This work investigates the potential of geothermal energy production beneath existing deep mines, providing insights for enhancing geothermal project design. Utilizing thermo-hydro-mechanical modeling, we assess the effects of cold water injection on the geothermal system long-term mechanical stability and the temperature distribution within the mine drifts. Additionally, the Distance-based Global Sensitivity Analysis (DGSA) method is implemented to evaluate the sensitivity of model parameters, offering direction for model optimization. The results of our analysis are summarized as follows:

1. Thermal stress significantly impacts the stability of drifts during cold water injection, with poroelastic stress being predominant at the onset of geothermal operation. These stresses lead to a decrease in stability, despite a temporary increase in stability at the base of the drift at the initial stages of the operation.
2. The relative location of the geothermal and mine systems is crucial for achieving satisfactory performance of the systems. Injection rate and temperature, along with rock properties such as thermal expansion coefficient, permeability, Young's modulus, and heat capacity, are critical in dictating the system behavior.
3. DGSA-based optimization approach proves to be effective in significantly enhancing system performance.
4. For the DGSA analysis involving 14 parameters, a sample size of 800 is identified as optimal, balancing comprehensive parameter sensitivity identification and computational efficiency.

The insights gained from this study significantly enhance the design and optimization of subsurface models, particularly for geothermal

energy applications. Our findings could lead to safer, more sustainable subsurface renewable energy operations.

CRediT authorship contribution statement

Le Zhang: Writing – review & editing, Writing – original draft, Visualization, Validation, Software, Resources, Methodology, Data curation, Conceptualization. **Anne-Catherine Dieudonné:** Writing – review & editing, Visualization, Supervision, Software, Validation, Formal Analysis, Methodology. **Alexandros Daniilidis:** Writing – review & editing, Visualization, Supervision, Software, Validation, Formal Analysis, Methodology, Conceptualization. **Longjun Dong:** Writing – review & editing, Supervision, Methodology, Conceptualization. **Wenzhuo Cao:** Writing – review & editing, Software, Methodology. **Robin Thibaut:** Writing – review & editing, Visualization, Software, Methodology, Conceptualization. **Luka Tas:** Writing – review & editing, Visualization, Software, Methodology. **Thomas Hermans:** Writing – review & editing, Supervision, Resources, Project administration, Methodology, Investigation, Funding acquisition, Formal analysis, Conceptualization.

Declaration of competing interest

The authors declare that they have no known competing financial interests or personal relationships that could have appeared to influence the work reported in this paper.

Data availability

Data will be made available on request.

Acknowledgment

This work was supported by Bilateral cooperation project between Flanders and China (grant number G0E5222N).

References

[1] Aghahosseini Arman, Breyer Christian. From hot rock to useful energy: A global estimate of enhanced geothermal systems potential. Appl Energy 2020;279:115769. http://dx.doi.org/10.1016/j.apenergy.2020.115769.

[2] Limberger Jon, Boxem Thijs, Pluymaekers Maarten, Bruhn David, Manzella Adele, Calcagno Philippe, Beekman Fred, Cloetingh Sierd, van Wees Jan-Diederik. Geothermal energy in deep aquifers: A global assessment of the resource base for direct heat utilization. Renew Sustain Energy Rev 2018;82:961–75. http://dx.doi.org/10.1016/j.rser.2017.09.084.

[3] Huang Yonghui, Kong Yanlong, Cheng Yuanzhi, Zhu Chuanqing, Zhang Jixiong, Wang Jiyang. Evaluating the long-term sustainability of geothermal energy utilization from deep coal mines. Geothermics 2023;107:102584. http://dx.doi.org/10.1016/j.geothermics.2022.102584.

[4] Guo Pingye, He Manchao, Zheng Liange, Zhang Na. A geothermal recycling system for cooling and heating in deep mines. Appl Therm Eng 2017;116:833–9. http://dx.doi.org/10.1016/j.applthermaleng.2017.01.116.

[5] CAI Mei-feng, MA Ming-hui, PAN Ji-liang, XI Xun, GUO Qi-feng. Co-mining of mineral and geothermal resources: a state-of-the-art review and future perspectives. Chin J Eng 2022;44(10):1669–81. http://dx.doi.org/10.13374/j.issn2095-9389.2022.08.24.001.

[6] Chu Zhaoxiang, Dong Kaijun, Gao Penghui, Wang Yijiang, Sun Qin. Mine-oriented low-enthalpy geothermal exploitation: A review from spatio-temporal perspective. Energy Convers Manage 2021;237:114123. http://dx.doi.org/10.1016/j.enconman.2021.114123.

[7] Matthes Ralph, Schreyer Jochen. Remediation of the old wismut-shaft 302 in marienberg and installation of a technical plant for geothermic mine water use (Ore Mountains, Germany). In: Proc. int.'mine water association symposium–water in mining environments', Cagliari, Italy. 2007, p. 227–31. http://dx.doi.org/10.5194/hess-2020-202-rc1.

[8] Kranz Kathrin, Dillenardt Julia. Mine water utilization for geothermal purposes in Freiberg, Germany: determination of hydrogeological and thermophysical rock parameters. Mine Water Environ 2010;29:68–76. http://dx.doi.org/10.1007/s10230-009-0094-4.

[9] Verhoeven René, Willems Eric, Harcouët-Menou Virginie, De Boever Eva, Hiddes Louis, Op't Veld Peter, Demollin Elianne. Minewater 2.0 project in heerlen the netherlands: transformation of a geothermal mine water pilot project into a full scale hybrid sustainable energy infrastructure for heating and cooling. Energy Procedia 2014;46:58–67. http://dx.doi.org/10.1016/j.egypro.2014.01.158.

[10] Peralta Ramos Esmeralda, Breede Katrin, Falcone Gioia. Geothermal heat recovery from abandoned mines: a systematic review of projects implemented worldwide and a methodology for screening new projects. Environ Earth Sci 2015;73:6783–95. http://dx.doi.org/10.1007/s12665-015-4285-y.

[11] Jardón Santiago, Ordóñez Almudena, Álvarez Rodrigo, Cienfuegos Pablo, Loredo Jorge. Mine water for energy and water supply in the central coal basin of asturias (Spain). Mine Water Environ 2013;32(2):139–51. http://dx.doi.org/10.1007/s10230-013-0224-x.

[12] Schubert JP, McDaniel MJ. Using mine waters for heating and cooling. In: Proceedings, 1st international mine water congress. 1982, p. 63–82.

[13] Guo Pingye, Zhu Guolong, He Manchao. HEMS technique for heat-harm control and geo-thermal utilization in deep mines. Int J Coal Sci Technol 2014;1(3):289–96. http://dx.doi.org/10.1007/s40789-014-0036-z.

[14] He Man-chao. Application of HEMS cooling technology in deep mine heat hazard control. Min Sci Technol (China) 2009;19(3):269–75. http://dx.doi.org/10.1016/s1674-5264(09)60051-x.

[15] Xu Yu, Li Zijun, Chen Yin, Jia Mintao, Zhang Mengsheng, Li Rongrong. Synergetic mining of geothermal energy in deep mines: An innovative method for heat hazard control. Appl Therm Eng 2022;210:118398. http://dx.doi.org/10.1016/j.applthermaleng.2022.118398.

[16] Xu Yu, Li Zijun, Tao Ming, Jalilinasrabady Saeid, Wang Junjian, Li Gang, Zhong Kaiqi. An investigation into the effect of water injection parameters on synergetic mining of geothermal energy in mines. J Clean Prod 2023;382:135256. http://dx.doi.org/10.1016/j.jclepro.2022.135256.

[17] Dong Longjun, Zhang Yihan, Wang Lichang, Wang Lu, Zhang Shen. Temperature dependence of mechanical properties and damage evolution of hot dry rocks under rapid cooling. J Rock Mech Geotech Eng 2024;16(2):645–60. http://dx.doi.org/10.1016/j.jrmge.2023.08.014.

[18] Zhang Yuliang, Zhao Gao-Feng. A global review of deep geothermal energy exploration: from a view of rock mechanics and engineering. Geomech Geophys Geo-Energy Geo-Resour 2020;6(1):4. http://dx.doi.org/10.1007/s40948-019-00126-z.

[19] Luo W, Kottsova A, Vardon PJ, Dieudonné AC, Brehme M. Mechanisms causing injectivity decline and enhancement in geothermal projects. Renew Sustain Energy Rev 2023;185:113623. http://dx.doi.org/10.1016/j.rser.2023.113623.

[20] Pandey SN, Vishal Vikram, Chaudhuri A. Geothermal reservoir modeling in a coupled thermo-hydro-mechanical-chemical approach: A review. Earth-Sci Rev 2018;185:1157–69. http://dx.doi.org/10.1016/j.earscirev.2018.09.004.

[21] Huang Y, Lei Z, Lipnikov K, Moulton JD, Sweeney MR, Hyman JD, Knight E, Stauffer PH. Modeling coupled thermo-hydro-mechanical-chemical processes in subsurface geological media. In: ARMA US rock mechanics/geomechanics symposium. ARMA; 2023, p. ARMA–2023. http://dx.doi.org/10.56952/arma-2023-0320.

[22] Watanabe Norihiro, Wang Wenqing, McDermott Christopher I, Taniguchi Takeo, Kolditz Olaf. Uncertainty analysis of thermo-hydro-mechanical coupled processes in heterogeneous porous media. Comput Mech 2010;45:263–80. http://dx.doi.org/10.1007/s00466-009-0445-9.

[23] Daniilidis Alexandros, Saeid Sanaz, Doonechaly Nima Gholizadeh. The fault plane as the main fluid pathway: Geothermal field development options under subsurface and operational uncertainty. Renew Energy 2021;171:927–46. http://dx.doi.org/10.1016/j.renene.2021.02.148.

[24] Wang Yang, Voskov Denis, Daniilidis Alexandros, Khait Mark, Saeid Sanaz, Bruhn David. Uncertainty quantification in a heterogeneous fluvial sandstone reservoir using GPU-based Monte Carlo simulation. Geothermics 2023;114:102773. http://dx.doi.org/10.1016/j.geothermics.2023.102773.

[25] Daniilidis Alexandros, Nick Hamidreza M, Bruhn David F. Interdependencies between physical, design and operational parameters for direct use geothermal heat in faulted hydrothermal reservoirs. Geothermics 2020;86:101806. http://dx.doi.org/10.1016/j.geothermics.2020.101806.

[26] Hermans Thomas, Goderniaux Pascal, Jougnot Damien, Fleckenstein Jan, Brunner Philip, Nguyen Frédéric, Linde Niklas, Huisman Johan Alexander, Bour Olivier, Lopez Alvis Jorge, et al. Advancing measurements and representations of subsurface heterogeneity and dynamic processes: towards 4D hydrogeology. Hydrol Earth Syst Sci Discuss 2022;2022:1–55. http://dx.doi.org/10.5194/hess-27-255-2023.

[27] Guo Pingye, Zheng Liange, Sun Xiaoming, He Manchao, Wang Yanwei, Shang Jingshi. Sustainability evaluation model of geothermal resources in abandoned coal mine. Appl Therm Eng 2018;144:804–11. http://dx.doi.org/10.1016/j.applthermaleng.2018.06.070.

[28] Aliyu Musa D, Chen Hua-Peng. Sensitivity analysis of deep geothermal reservoir: Effect of reservoir parameters on production temperature. Energy 2017;129:101–13. http://dx.doi.org/10.1016/j.energy.2017.04.091.

[29] Sun Zhi-xue, Zhang Xu, Xu Yi, Yao Jun, Wang Hao-xuan, Lv Shuhuan, Sun Zhilei, Huang Yong, Cai Ming-yu, Huang Xiaoxue. Numerical simulation of the heat extraction in EGS with thermal-hydraulic-mechanical coupling method based on discrete fractures model. Energy 2017;120:20–33. http://dx.doi.org/10.1016/j.energy.2016.10.046.

[30] Yao Jun, Zhang Xu, Sun Zhixue, Huang Zhaoqin, Liu Junrong, Li Yang, Xin Ying, Yan Xia, Liu Wenzheng. Numerical simulation of the heat extraction in 3D-EGS with thermal-hydraulic-mechanical coupling method based on discrete fractures model. Geothermics 2018;74:19–34. http://dx.doi.org/10.1016/j.geothermics.2017.12.005.

[31] Song Xiaomeng, Zhang Jianyun, Zhan Chesheng, Xuan Yunqing, Ye Ming, Xu Chonggang. Global sensitivity analysis in hydrological modeling: Review of concepts, methods, theoretical framework, and applications. J Hydrol 2015;523:739–57. http://dx.doi.org/10.1016/j.jhydrol.2015.02.013.

[32] Fenwick Darryl, Scheidt Céline, Caers Jef. Quantifying asymmetric parameter interactions in sensitivity analysis: application to reservoir modeling. Math Geosci 2014;46:493–511. http://dx.doi.org/10.1007/s11004-014-9530-5.

[33] Park Jihoon, Yang Guang, Satija Addy, Scheidt Céline, Caers Jef. DGSA: A matlab toolbox for distance-based generalized sensitivity analysis of geoscientific computer experiments. Comput Geosci 2016;97:15–29. http://dx.doi.org/10.1016/j.cageo.2016.08.021.

[34] Athens Noah D, Caers Jef K. A Monte Carlo-based framework for assessing the value of information and development risk in geothermal exploration. Appl Energy 2019;256:113932. http://dx.doi.org/10.1016/j.apenergy.2019.113932.

[35] Hermans Thomas, Nguyen Frédéric, Klepikova Maria, Dassargues Alain, Caers Jef. Uncertainty quantification of medium-term heat storage from short-term geophysical experiments using Bayesian evidential learning. Water Resour Res 2018;54(4):2931–48. http://dx.doi.org/10.1002/2017wr022135.

[36] Li Xinxin, Li Chengyu, Gong Wenping, Zhang Yanjie, Wang Junchao. Probabilistic analysis of heat extraction performance in enhanced geothermal system based on a DFN-based modeling scheme. Energy 2023;263:125674. http://dx.doi.org/10.1016/j.energy.2022.125674.

[37] Kim Seunghee, Hosseini Seyyed A. Hydro-thermo-mechanical analysis during injection of cold fluid into a geologic formation. Int J Rock Mech Min Sci 2015;77:220–36. http://dx.doi.org/10.1016/j.ijrmms.2015.04.010.

[38] COMSOL. COMSOL multiphysics reference manual. 2024, URL https://doc.comsol.com/6.2/docserver/#!/com.comsol.help.comsol/helpdesk/helpdesk.html.

[39] Vilarrasa Víctor, Olivella Sebastià, Carrera Jesús, Rutqvist Jonny. Long term impacts of cold CO2 injection on the caprock integrity. Int J Greenh Gas Control 2014;24:1–13. http://dx.doi.org/10.1016/j.ijggc.2014.02.016.

[40] Thibaut Robin, Laloy Eric, Hermans Thomas. A new framework for experimental design using Bayesian evidential learning: The case of wellhead protection area. J Hydrol 2021;603:126903. http://dx.doi.org/10.1016/j.jhydrol.2021.126903.

[41] Xue Yi, Liu Shuai, Chai Junrui, Liu Jia, Ranjith PG, Cai Chengzheng, Gao Feng, Bai Xue. Effect of water-cooling shock on fracture initiation and morphology of high-temperature granite: Application of hydraulic fracturing to enhanced geothermal systems. Appl Energy 2023;337:120858. http://dx.doi.org/10.1016/j.apenergy.2023.120858.

[42] Liu Guihong, Pu Hai, Zhao Zhihong, Liu Yanguang. Coupled thermo-hydro-mechanical modeling on well pairs in heterogeneous porous geothermal reservoirs. Energy 2019;171:631–53. http://dx.doi.org/10.1016/j.energy.2019.01.022.

[43] Chen Mingjie, Tompson Andrew FB, Mellors Robert J, Abdalla Osman. An efficient optimization of well placement and control for a geothermal prospect under geological uncertainty. Appl Energy 2015;137:352–63. http://dx.doi.org/10.1016/j.apenergy.2014.10.036.

[44] Perzan Z, Babey T, Caers J, Bargar JR, Maher K. Local and global sensitivity analysis of a reactive transport model simulating floodplain redox cycling. Water Resour Res 2021;57(12):e2021WR029723. http://dx.doi.org/10.1029/2021wr029723.

[45] Scheidt Céline, Li Lewis, Caers Jef. Quantifying uncertainty in subsurface systems, vol. 236, John Wiley & Sons; 2018, http://dx.doi.org/10.1002/9781119325888.ch8.

[46] Sackfield A, Hills DA, Nowell D. Mechanics of elastic contacts. Elsevier; 1993, http://dx.doi.org/10.1016/c2009-0-24029-3.

[47] Glassley William E. Geothermal energy: renewable energy and the environment. CRC Press; 2014, http://dx.doi.org/10.1201/b17521.

[48] Wang Jiacheng, Zhao Zhihong, Liu Guihong, Xu Haoran. A robust optimization approach of well placement for doublet in heterogeneous geothermal reservoirs using random forest technique and genetic algorithm. Energy 2022;254:124427. http://dx.doi.org/10.1016/j.energy.2022.124427.

[49] Thibaut Robin, Compaire Nicolas, Lesparre Nolwenn, Ramgraber Maximilian, Laloy Eric, Hermans Thomas. Comparing well and geophysical data for temperature monitoring within a Bayesian experimental design framework. Water Resour Res 2022;58(11):e2022WR033045. http://dx.doi.org/10.1029/2022WR033045.

[50] Zhang Yuliang, Zhao Gao-Feng. A multiphysics method for long-term deformation analysis of reservoir rock considering thermal damage in deep geothermal engineering. Renew Energy 2023;204:432–48. http://dx.doi.org/10.1016/j.renene.2023.01.026.

[51] Jain Gaurav, Singh Aditya. An elastoplastic semi-analytical solution for enhanced geothermal wellbore stability considering temperature-sensitive failure criterion. Geothermics 2024;121:103046. http://dx.doi.org/10.1016/j.geothermics.2024.103046.